



HAL
open science

Experimental and numerical assessment of deterministic nonlinear ocean waves prediction algorithms using non-uniformly sampled wave gauges

Nicolas Desmars, Félicien Bonnefoy, Stéphan T. Grilli, Guillaume Ducrozet, Yves Perignon, Charles-Antoine Guérin, Pierre Ferrant

► To cite this version:

Nicolas Desmars, Félicien Bonnefoy, Stéphan T. Grilli, Guillaume Ducrozet, Yves Perignon, et al.. Experimental and numerical assessment of deterministic nonlinear ocean waves prediction algorithms using non-uniformly sampled wave gauges. *Ocean Engineering*, 2020, 212, pp.107659. 10.1016/j.oceaneng.2020.107659 . hal-02880225

HAL Id: hal-02880225

<https://hal.science/hal-02880225>

Submitted on 2 Sep 2020

HAL is a multi-disciplinary open access archive for the deposit and dissemination of scientific research documents, whether they are published or not. The documents may come from teaching and research institutions in France or abroad, or from public or private research centers.

L'archive ouverte pluridisciplinaire **HAL**, est destinée au dépôt et à la diffusion de documents scientifiques de niveau recherche, publiés ou non, émanant des établissements d'enseignement et de recherche français ou étrangers, des laboratoires publics ou privés.



Distributed under a Creative Commons Attribution - NonCommercial 4.0 International License

Experimental and numerical assessment of deterministic nonlinear ocean waves prediction algorithms using non-uniformly sampled wave gauges

N. Desmars ^{a,*}, F. Bonnefoy ^a, S.T. Grilli ^b, G. Ducrozet ^a, Y. Perignon ^a, C.-A. Guérin ^c, P. Ferrant ^a

^a *École Centrale de Nantes, LHEEA Res. Dept. (ECN and CNRS), 44321 Nantes, France*

^b *Department of Ocean Engineering, University of Rhode Island, Narragansett, RI 02882, USA*

^c *Université de Toulon, Aix-Marseille Université, IRD, CNRS-INSU, Mediterranean Institute of Oceanography (MIO UM 110), 83957 La Garde, France*

We assess the capability of fast wave models to deterministically predict nonlinear ocean surface waves from non-uniformly distributed data such as sampled from an optical ocean sensor. Linear and weakly nonlinear prediction algorithms are applied to long-crested irregular waves based on a set of laboratory experiments and corresponding numerical simulations. An array of wave gauges is used for data acquisition, representing the typical spatial sampling an optical sensor (e.g., LIDAR) would make at grazing incidence. Predictions of the weakly nonlinear Improved Choppy Wave Model are compared to those of the Linear Wave Theory with and without a nonlinear dispersion relationship correction. Wave models are first inverted based on gauge data which provides the initial model parameters, then propagated to issue a prediction. We find that the wave prediction accuracy converges with the amount of input data used in the inversion. When waves are propagated in the models, correctly modeling the nonlinear wave phase velocity provides the main improvement in accuracy, while including nonlinear wave shape effects only improves surface elevation representation in the spatio-temporal region where input data are acquired. Surface slope prediction accuracy, however, strongly depends on the appropriate nonlinear wave shape modeling.

1. Introduction

The availability of real-time phase-resolved wave fields is key for the optimization of a vast range of marine applications. The prediction and control of the wave-induced motion is crucially important to extend the operational envelope and optimal maneuvering of many surface vessels, such as to stabilize aircraft or helicopter carriers during takeoff/landing manoeuvres, ships during ship-to-ship transfer, or to perform installation and maintenance operations on marine structures. For ocean renewable energy harvesting systems, advance knowledge of incoming waves conditions the performances of control strategies. For instance, it is shown that the optimal control of wave energy converters relying on wave-to-wave predictions significantly improves their efficiency (Li et al., 2012). Also, the life-time of floating wind turbines could be increased by mitigating fatigue loads through appropriate control of the structure motions induced by wave loads (Ma et al., 2018).

The deterministic prediction of ocean wave fields requires inverting a model describing the wave dynamics based on a set of observations, i.e., measurements that contain information about the wave geometry and kinematics (e.g., Nouguier et al., 2014). Based on such an inversion

(i.e., nowcast), the properly parameterized wave model can then be used to propagate the wave field forward in time (i.e., forecast) to the area of interest. Note that the later can itself be in motion (e.g., a moving ship).

X-band radars, such as WaMoS II developed by OceanWaveS GmbH[™] (Hilmer and Thornhill, 2015), the prediction systems of Next Ocean[™] (Naaijen et al., 2018), or FutureWaves[™] (Kusters et al., 2016), have been used to generate large spatio-temporal data sets of wave elevations surrounding the structure upon which they are mounted. Such radars make use of the backscattered signal resulting from the Bragg resonance between the radar microwaves (~ 3 cm wavelength) and short-wavelength capillary-gravity waves (~ 1.5 cm wavelength) covering the ocean surface due to wind generation. Hydrodynamic and tilt modulations of such short ripples by longer gravity waves carrying them, that affect the backscattered signal, allow inverting for surface elevations by means of a modulation transfer function (MTF) (Nieto Borge et al., 2004), provided that a calibration is enabling a retrofit on this MTF in the measurement chain. This technology has been successfully implemented in commercial products (Hilmer and Thornhill, 2015; Kusters et al., 2016; Naaijen et al., 2018).

* Corresponding author.

E-mail address: nicolas.desmars@protonmail.com (N. Desmars).

Similar data sets can be obtained by the way of LIDAR (Light Detection and Ranging) cameras (Belmont et al., 2007; Grilli et al., 2011; Noguier et al., 2014; Kabel et al., 2019), which operate in the visible light (e.g., green; 532 nm wavelength). Instead of using modulation properties of Bragg waves to estimate gravity waves characteristics, LIDAR cameras provide direct geo-referenced measurements of free surface elevations, computed based on laser beam travel times. One advantage of this technique, as compared to X-band radars, is the higher spatial resolution resulting from the smaller divergence of the laser beams compared to the microwave beams (Sviridov, 1993), providing a more accurate phase resolved (instantaneous) measurement of the ocean surface.

When mounted on an ocean structure or surface vessel to remotely measure ocean surface elevations, both X-band radar and LIDAR camera have limitations resulting from the grazing incidence angles of the beams. First, it will cause wave shadowing effects, leading data sets acquired by these systems to exhibit spatial gaps behind illuminated wave fronts which have an area increasing with the distance from the sensor. Second, assuming a uniform distribution of beams over the sensor's aperture angles, the density of the measurement points geometrically decreases with the distance from the sensor. In the case of X-band radars, shadowing effects are used to generate a shadowing mask that is implemented in the MTF used for wave inversion (Nieto Borge et al., 2004). For LIDAR cameras, the lack of information in the shadowed area can be compensated for by using spatio-temporal data sets, i.e., at a slightly later time, shadowed areas without measurement points can become illuminated due to wave motion. This, however, also requires performing a spatio-temporal wave field inversion (Grilli et al., 2011; Noguier et al., 2014; Desmars et al., 2018). In addition to generating spatial gaps, shadowing effects cause laser beams to hit the ocean surface at unknown horizontal locations, leading the measurement points to be distributed over an a priori unknown unstructured grid. These properties, together with the non-periodicity of observations, prevent using standard signal-processing techniques based on Fourier decomposition in the wave inversion, unless a pre- or post-processing method is used (e.g., interpolation, end-matching, filtering).

Due to real-time constraints, i.e., sufficient computational efficiency, existing deterministic wave prediction systems have typically used models based on linear wave theory (LWT) (Hilmer and Thornhill, 2015; Kusters et al., 2016; Naaijen et al., 2018). However, this limits their applicability to sea states with a small characteristic steepness, and further assumes that: (i) bound waves (i.e., harmonic waves that do not obey the dispersion relation) can be neglected, and (ii) the space and time scales of observations and the prediction horizon do not allow time-dependent nonlinear wave-wave interactions (e.g., nonlinear phase shift) to significantly affect wave dynamics. Whenever these limitations are not met, the accurate prediction of ocean surface waves will require modeling weakly or fully nonlinear wave properties.

Weakly nonlinear models have been developed and used for wave simulation and prediction based on expanding Eulerian wave properties up to the second-order in wave steepness (e.g., Zhang et al., 1996, 1999), which for instance allows separating free- and bound-wave components in wave measurements. A model based on the Modified NonLinear Schrödinger (MNLS) equation, which simulates third-order wave properties such as phase speed, was used to predict bichromatic waves (Trulsen and Stansberg, 2001), then extended to both one-directional and directional irregular seas (Simanesev et al., 2017). The latter study showed that the MNLS equation is able to provide satisfactory predictions of long-crested irregular waves, but the lack of directional input data prevented properly estimating its prediction performance for short-crested waves with increasing directional spread. Higher-order wave models based on the High-Order Spectral (HOS) method were also applied for nonlinear prediction of ocean surfaces (e.g., Wu, 2004; Blondel et al., 2010; Qi et al., 2018a). Based on a pseudo-spectral approach, this method solves the nonlinear free

surface boundary conditions to an arbitrary order for a velocity potential, and allows to simulate the propagation of any wave fields over large space and time scales with a high accuracy. Predictions of long-crested irregular waves using both HOS, LWT and nonlinear Schrödinger approaches were recently compared (Klein et al., 2020), showing that the appropriate modeling of nonlinear dispersion effects plays a significant role from moderate to high wave steepness, with HOS being the most accurate prediction model. The main counterpoint of HOS is its initialization process that necessitates a high number of operations, exponentially increasing with its order of nonlinearity. Recent works have been carried out on improved assimilation methods for HOS to be adequate for real-time prediction (Köllisch et al., 2018; Fujimoto and Waseda, 2020).

In this study, we apply and experimentally validate a wave reconstruction and prediction algorithm based on the recently developed Improved Choppy Wave Model (ICWM) (Guérin et al., 2019), which extends with higher-order corrections the weakly nonlinear Lagrangian Choppy Wave Model (Noguier et al., 2009), which was used in our earlier work on ocean wave reconstruction algorithms based on LIDAR camera data (Grilli et al., 2011; Noguier et al., 2014).

The paper is organized as follows. Section 2 provides a description of the wave models that are used in this study, namely the LWT, the ICWM and a linear wave model corrected with a nonlinear dispersion relation. Section 3 details the data assimilation procedure that is employed here, as well as key aspects relative to the determination of the accessible prediction zone. Section 4 describes the experimental and numerical modeling setups used in our applications, together with an analysis of the experimental data perturbations, followed by definitions of the prediction misfit indicators used in this study. Section 5 investigates the sensitivity of the proposed prediction algorithms to assimilation parameters. Their accuracy is finally discussed in Section 6.

2. Wave models

While it is desirable to account for the nonlinearity of ocean waves, the development of fast methods for the real-time reconstruction and prediction of nonlinear sea states cannot be easily or efficiently achieved using complex (i.e., highly nonlinear) wave models, such as based on a HOS method (e.g., Wu, 2004; Blondel et al., 2010; Qi et al., 2018a). Instead, the wave model used to this effect should be able to properly account for salient nonlinear effects in the propagation of the considered wave fields, while being sufficiently efficient for providing real-time predictions. Here, we consider and compare two wave models: one based on linear wave theory (LWT), and a weakly nonlinear wave model, referred to as Choppy Wave Model (CWM), derived in an explicit, efficient, Lagrangian formalism. The improved form of CWM, referred to as Improved Choppy Wave Model (ICWM) (Guérin et al., 2019) is used in the present applications. Both models provide an analytical expression of the free surface elevation, which can be efficiently initiated (the assimilation procedure is detailed in Section 3.1) and propagated forward in time to forecast the future state of a given wave field, the latter being simply obtained by increasing the value of time in the formulation. We limit our developments to the deep water assumption, but the extension to intermediate depth is straightforward.

2.1. Linear wave theory

LWT refers here to the equations derived from the classical Eulerian approach, for an inviscid, incompressible fluid with an irrotational motion, linearized with respect to the wave steepness. Let us consider a Cartesian coordinate system (x, y, z) , with the x - and y -horizontal axes located at the mean water surface and the z -axis being vertical and positive upward. Under LWT, a generic irregular ocean surface (wave field) is simply represented as the superposition of $n = 1, \dots, N$ individual harmonic wave components propagating in the horizontal

plane $\mathbf{r} = (x, y)$ in direction θ_n with respect to the x -axis, of amplitude A_n and angular frequency ω_n , following

$$\eta^{\text{lin}}(\mathbf{r}, t) = \sum_{n=1}^N A_n \cos(\mathbf{k}_n \cdot \mathbf{r} - \omega_n t - \varphi_n), \quad (1)$$

where t is time, φ_n are phases, and $\mathbf{k}_n = k_n \hat{\mathbf{k}}_n = (k_n \cos \theta_n, k_n \sin \theta_n)$ and $k_n = 2\pi/\lambda_n = |\mathbf{k}_n|$ are wavenumber vectors and wavenumbers, respectively (with λ_n the wavelength), with the latter found as $k_n = \omega_n^2/g$ based on the deep water dispersion relationship, and g the acceleration of gravity. To simplify later mathematical developments, the free surface will be equivalently described as

$$\eta^{\text{lin}}(\mathbf{r}, t) = \sum_{n=1}^N (a_n \cos \psi_n + b_n \sin \psi_n), \quad (2)$$

in which $\psi_n = \mathbf{k}_n \cdot \mathbf{r} - \omega_n t$ are spatio-temporal phases, and $(a_n, b_n) = (A_n \cos \varphi_n, A_n \sin \varphi_n)$ are wave parameters describing the ocean surface.

2.2. Improved choppy wave model

The CWM was derived based on a first-order Lagrangian description of water particle motions on the free surface (Nouguier et al., 2009), and thus corresponds, for a periodic wave, to the classical Gerstner wave model (Gerstner, 1809). The CWM provides results that include features from a higher-order Eulerian wave theory (e.g., second-order Stokes theory), but the wave phase speed is still that given by LWT. A recent improvement of the CWM was proposed to account for higher-order nonlinear effects, in particular on the wave phase speed, without requiring a full second-order Lagrangian description (Guérin et al., 2019). The resulting wave model ICWM is used in the present work. Using a formalism similar to that introduced in the previous section, ICWM represents the free surface elevation $z(\mathbf{r}_0, t)$ as a function of time, for water particles initially located at \mathbf{r}_0 on the still water level at rest as

$$\begin{cases} \mathbf{r}(\mathbf{r}_0, t) = \mathbf{r}_0 + \sum_{n=1}^N \hat{\mathbf{k}}_n (-a_n \sin \tilde{\psi}_n + b_n \cos \tilde{\psi}_n) + \mathbf{U}_{s0} t, & (a) \\ z(\mathbf{r}_0, t) = \sum_{n=1}^N (a_n \cos \tilde{\psi}_n + b_n \sin \tilde{\psi}_n) + \sum_{n=1}^N \frac{1}{2} (a_n^2 + b_n^2) k_n, & (b) \end{cases} \quad (3)$$

where $\tilde{\psi}_n = \mathbf{k}_n \cdot \mathbf{r}_0 - \tilde{\omega}_n t$ denote phases of wave components, $\tilde{\omega}_n = \omega_n - \frac{1}{2} \mathbf{k}_n \cdot \mathbf{U}_{s0}$ modified angular frequencies, and $\mathbf{U}_{s0} = \sum_{n=1}^N (a_n^2 + b_n^2) \omega_n \mathbf{k}_n$ the free surface Stokes drift vector. The last term in Eq. (3a) and in the modified angular frequency equation are nonlinear corrections added to the standard CWM which account for Stokes drift effects on the free surface. The last term in Eq. (3b) accounts for a correction of the mean surface level.

Typical measurements of ocean surfaces, such as with an optical system, are made at irregularly distributed locations defined in a reference coordinate system, hence these are Eulerian measurements. The wave model used to reconstruct the ocean surface must thus be able to use similar information, which makes the above Lagrangian form of ICWM not directly usable. Hence, an approximate Eulerian model, equivalent to ICWM is derived in the following, introducing an approximation similar to that made of the CWM (Nouguier et al., 2009), for which an efficient algorithm was developed based on computing horizontal displacements of a reference linear surface, using efficient Riesz and spatial Fourier transforms.

An explicit relationship between \mathbf{r} and z in Eqs. (3a) and (3b) could be derived by performing a Taylor series expansion of particle vertical locations z around their instantaneous horizontal location \mathbf{r} , thus providing $z(\mathbf{r})$. In this case, however, successive Eulerian orders of expansion lose the Lagrangian formulation's simplicity, which makes the model inefficient. Here, we first modify Eqs. (3a) and (3b) by implicitly incorporating the particle horizontal shift into a modified angular frequency $\tilde{\phi}_n$, thus replacing \mathbf{r}_0 by $\mathbf{r}'_0 = \mathbf{r}_0 - \mathbf{U}_{s0} t$, leading to

$$\begin{cases} \mathcal{R}(\mathbf{r}_0, t) = \mathbf{r}(\mathbf{r}'_0, t) = \mathbf{r}_0 + \mathcal{D}(\mathbf{r}_0) = \mathbf{r}_0 + \sum_{n=1}^N \hat{\mathbf{k}}_n (-a_n \sin \tilde{\phi}_n + b_n \cos \tilde{\phi}_n), \\ \mathcal{Z}(\mathbf{r}_0, t) = z(\mathbf{r}'_0, t) = \sum_{n=1}^N (a_n \cos \tilde{\phi}_n + b_n \sin \tilde{\phi}_n) + \sum_{n=1}^N \frac{1}{2} (a_n^2 + b_n^2) k_n, \end{cases}$$

where $\tilde{\phi}_n = \mathbf{k}_n \cdot \mathbf{r}_0 - \tilde{\omega}_n t$ and $\tilde{\omega}_n = \omega_n + \frac{1}{2} \mathbf{k}_n \cdot \mathbf{U}_{s0}$. Then, as for the CWM (Nouguier et al., 2009), a simple method for numerically evaluating ICWM surface elevation at any spatial point is derived by computing the particle vertical displacement at its instantaneous rather than its reference location. Earlier work has shown (Grilli et al., 2011; Nouguier et al., 2014) that errors due to this approximation are on the order of the mean square surface slope (i.e., the second-order moment of the wave spectrum $\int_0^{+\infty} k^2 S_\eta(k) dk$), which is expected to be small compared to other sources of error in the ocean surface reconstruction process. Hence, assuming

$$\mathcal{Z}(\mathbf{r}_0) = \mathcal{Z}(\mathcal{R} - \mathcal{D}(\mathbf{r}_0)) \approx \mathcal{Z}(\mathcal{R} - \mathcal{D}(\mathcal{R})) = \eta^{\text{nl}}(\mathcal{R}), \quad (5)$$

Eq. (4) yields an explicit approximate nonlinear free surface elevation η^{nl} at any spatial point \mathbf{r} as

$$\eta^{\text{nl}}(\mathbf{r}, t) = \sum_{n=1}^N \left(a_n \cos \Psi_n + b_n \sin \Psi_n + \frac{1}{2} (a_n^2 + b_n^2) k_n \right), \quad (6)$$

$$\Psi_n = \mathbf{k}_n \cdot \left[\mathbf{r} - \sum_{i=1}^N \hat{\mathbf{k}}_i (-a_i \sin \tilde{\phi}_i + b_i \cos \tilde{\phi}_i) \right] - \tilde{\omega}_n t,$$

where the modified phases are now computed as $\tilde{\phi}_i = \mathbf{k}_i \cdot \mathbf{r} - \tilde{\omega}_i t$.

2.3. Linear wave theory with corrected dispersion relation

To quantify effects of nonlinear wave phase corrections on our wave prediction results, independently of the wave shape asymmetry represented in the ICWM, we will evaluate the performance of a third wave model, referred to as LWT-CDR, which is based on LWT Eq. (2), but uses a dispersion relationship corrected by Stokes drift, as for the ICWM, i.e., the linear angular frequency $\omega_n(k)$ is replaced by its nonlinear equivalent $\tilde{\omega}_n(k)$. This yields the corrected linear free surface elevation

$$\eta^{\text{cl}}(\mathbf{r}, t) = \sum_{n=1}^N (a_n \cos \tilde{\phi}_n + b_n \sin \tilde{\phi}_n). \quad (7)$$

3. Methods

Model-based predictions rely on the model inversion from observations (measured data) for parameters specifying the initial conditions prior to model propagation. This model initialization step, referred to as the assimilation procedure, is detailed in this section for the three wave models presented previously. We then explain the method to determine theoretically the accessible spatio-temporal prediction zone from the assimilated data.

3.1. Data assimilation procedure

A standard method for assimilating wave elevation data is the variational approach (Blondel, 2009), in which a cost function F , representing the error between the ‘‘measured wave field’’ and its representation with a wave model, is minimized. Here, we assume that an a priori estimate of the solution is not available and statistical parameters of the aleatory error in observations (or free-surface elevation measurements) are stationary, i.e., they are not functions of time or space. Accordingly, similar to earlier work (Grilli et al., 2011; Nouguier et al., 2014), the cost function is expressed as the mean square of the difference between spatio-temporal ocean observations and their model representation as

$$F(\mathbf{p}) = \frac{1}{2} \sum_{k=1}^K \sum_{j=1}^J (\eta_{jk}(\mathbf{p}) - \bar{\eta}_{jk})^2 = \frac{1}{2} \sum_{\ell=1}^L (\eta_\ell(\mathbf{p}) - \bar{\eta}_\ell)^2, \quad (8)$$

in which $\mathbf{p} = \{a_n, b_n\}$ ($n = 1, \dots, N$) is the control vector of $2N$ unknown model parameters, J and K are the number of spatial observations made at each observation time and the number of observation

times, respectively (hence, the total number of assimilated spatio-temporal observations is $J \times K = L$), $\bar{\eta}_{jk}$ (or $\bar{\eta}_{\ell}$) are free surface elevations measured at spatial locations r_j ($j = 1, \dots, J$) and times t_k ($k = 1, \dots, K$), and η_{jk} (or η_{ℓ}) are estimates of these computed with the wave model, i.e., with Eq. (2) for LWT, Eq. (7) for LWT-CDR, or Eq. (6) for ICWM.

Model parameters are obtained next, by minimizing the cost function with respect to these parameters and solving the system of equations

$$\left\{ \frac{\partial F}{\partial a_m} = 0, \quad \frac{\partial F}{\partial b_m} = 0 \right\} \iff A_{mn} p_n = B_m, \quad (9)$$

where $n, m \in \{1, \dots, N\}^2$, and $p_n = a_n$, $p_{N+n} = b_n$ constitute the unknown vector of $2N$ model parameters associated to wave components of predefined wavenumbers k_n . The set of wavenumbers k_n is distributed in $[k^{\min}, k^{\max}]$ following a decreasing logarithmic law, with $k^{\min, \max}$ defining the bandwidth of the reconstructed wave field (see Section 3.3 for details about how to choose $k^{\min, \max}$). Since the considered wave models have analytical formulations, the system of Eq. (9) can be explicitly expressed. Note that in practice, and to increase the accuracy of the parameter estimation, the number of observations used L is larger than the number of wave components N used to perform the wave model inversion. Hence, the optimal solution of an overdetermined system of equations is computed to assimilate data in the model, which can be done using a least squares method. Accordingly, to obtain an accurate solution, the larger the spatio-temporal region covered by the observations, the larger the number of degrees of freedom required in the wave model. In each application considered in the following, N will be adequately selected to satisfy this constraint.

3.1.1. Linear assimilation

Linear wave fields are reconstructed by computing the cost function Eq. (8) using the linear wave model Eq. (2). Thus, in the minimization Eq. (9), we get

$$\begin{aligned} A_{mn} &= \sum_{\ell=1}^L \cos \psi_{n\ell} \cos \psi_{m\ell}, & A_{m, N+n} &= \sum_{\ell=1}^L \sin \psi_{n\ell} \cos \psi_{m\ell}, \\ A_{N+m, n} &= \sum_{\ell=1}^L \cos \psi_{n\ell} \sin \psi_{m\ell}, & A_{N+m, N+n} &= \sum_{\ell=1}^L \sin \psi_{n\ell} \sin \psi_{m\ell}. \end{aligned} \quad (10)$$

and

$$B_m = \sum_{\ell=1}^L \bar{\eta}_{\ell} \cos \psi_{m\ell}, \quad B_{N+m} = \sum_{\ell=1}^L \bar{\eta}_{\ell} \sin \psi_{m\ell}, \quad (11)$$

where $\psi_{m\ell} = \mathbf{k}_m \cdot \mathbf{r}_{\ell} - \omega_m t_{\ell}$.

3.1.2. Nonlinear assimilation

Nonlinear wave fields are reconstructed by computing the cost function Eq. (8) using the ICWM Eq. (6). Thus, in the minimization Eq. (9), we now obtain

$$\begin{aligned} A_{mn} &= \sum_{\ell=1}^L \left(\cos \psi_{n\ell} + \frac{1}{2} a_n k_n \right) P_{m\ell}, & A_{m, N+n} &= \sum_{\ell=1}^L \left(\sin \psi_{n\ell} + \frac{1}{2} b_n k_n \right) P_{m\ell}, \\ A_{N+m, n} &= \sum_{\ell=1}^L \left(\cos \psi_{n\ell} + \frac{1}{2} a_n k_n \right) Q_{m\ell}, & A_{N+m, N+n} &= \sum_{\ell=1}^L \left(\sin \psi_{n\ell} + \frac{1}{2} b_n k_n \right) Q_{m\ell}, \end{aligned} \quad (12)$$

and

$$B_m = \sum_{\ell=1}^L \bar{\eta}_{\ell} P_{m\ell}, \quad B_{N+m} = \sum_{\ell=1}^L \bar{\eta}_{\ell} Q_{m\ell}, \quad (13)$$

in which

$$\begin{cases} P_{m\ell} = \cos \Psi_{m\ell} - k_m (a_m \sin \Psi_{m\ell} - b_m \cos \Psi_{m\ell}) \\ \quad \times \{ \sin \tilde{\phi}_{m\ell} - [k_m (a_m \cos \tilde{\phi}_{m\ell} + b_m \sin \tilde{\phi}_{m\ell}) + 1] \\ \quad \times a_m \omega_m k_m t_{\ell} \} + a_m k_m, \\ Q_{m\ell} = \sin \Psi_{m\ell} - k_m (a_m \sin \Psi_{m\ell} - b_m \cos \Psi_{m\ell}) \\ \quad \times \{ -\cos \tilde{\phi}_{m\ell} - [k_m (a_m \cos \tilde{\phi}_{m\ell} + b_m \sin \tilde{\phi}_{m\ell}) + 1] \\ \quad \times b_m \omega_m k_m t_{\ell} \} + b_m k_m. \end{cases} \quad (14)$$

Since both A_{mn} and B_m now depend on model parameters (a_n, b_n) , the system of Eq. (9) must be solved iteratively. Following Nougier et al. (2014), when solving for $p_n^{(q+1)}$ at iteration $q+1$, $A_{mn}^{(q)}$ and $B_m^{(q)}$ are computed based on wave parameters obtained at the previous iteration q . The solution is initialized at $q=0$ by computing $A_{mn}^{(0)}$ and $B_m^{(0)}$ as for the linear reconstruction, using Eqs. (10) and (11). Based on a relative error between $p_n^{(q)}$ and $p_n^{(q+1)}$ evaluated at each iteration $q+1$, convergence of the solution is typically achieved within a few to a few dozens iterations, depending on the wave steepness. This ensures a very efficient assimilation procedure in this nonlinear context.

As indicated above, a third system of equations is solved for wave parameters corresponding to the LWT-CDR (Eq. (7)). This formulation is not detailed here for the sake of conciseness.

3.1.3. Regularization of the inverse problem

In operative applications, the ocean reconstruction problem may become ill-conditioned due to practical constraints, such as the heterogeneous distribution of spatial observation points, the limited ocean area observed by the optical sensor, and the frequency and direction bandwidth cutoffs in the reconstructed wave field. Nevertheless, consistent results can be achieved, independently of the conditioning of the system matrix to invert (i.e., A_{mn}), by applying a Tikhonov regularization, in which the matrix inversion is replaced by the following minimization problem

$$\min \left(\|A_{mn} p_n - B_m\|^2 - \xi^2 \|p_n\|^2 \right), \quad (15)$$

where ξ denotes the regularization parameter. An optimal value of the regularization parameter can be found using the ‘‘L-curve’’ method, which consists in finding the ξ value corresponding to the point of maximal curvature (i.e., corner) of the parametric curve $(\log \|A_{mn} p_n - B_m\|, \log \|p_n\|)$. This method provides an optimal compromise between minimizing the residual error of the assimilation system and ensuring that the norm of the solution does not become too large. The L-curve corner can be determined analytically through solving a singular value decomposition problem (Calvetti et al., 2004; Hansen, 2000). Note that this procedure is equivalent to adding a constraint to the minimization problem, physically representing the total energy of the reconstructed wave spectrum, since the latter is proportional to the squared norm of p_n . In this case, $-\xi^2$ can simply be interpreted as a Lagrangian multiplier.

3.2. Accessible prediction zone from non-uniform observations

Earlier work has shown that the spatio-temporal region over which wave dynamics can be predicted based on a set of free surface measurements, is bounded (Wu, 2004; Naaijen et al., 2014; Qi et al., 2018b). When measurements are made using an optical system, at a specific sampling rate and over a given observation zone, this limits the amount of data that can be assimilated and used in the wave reconstruction process, yielding a reconstructed surface in space/time defined with finite frequency and direction bandwidths. In light of this, the sea-state prediction obtained by propagating the assimilated information is similarly limited to a spatio-temporal region referred to as prediction zone. In the following, we show how the latter can be estimated for a set of fixed surface observations of a one-directional wave field.

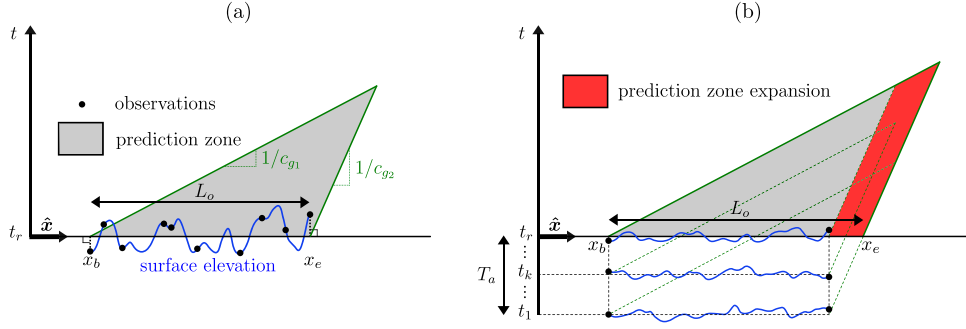


Fig. 1. Evolution of the wave prediction zone in time and space for the assimilation of: (a) spatial data and (b) spatio-temporal data (dash lines are prediction zones boundaries at time t_k ; the increase in the prediction zone relative to that of spatial only observations is highlighted in red); c_{g_1} and c_{g_2} denote the fastest and slowest group velocities transporting a significant amount of energy in the wave field, respectively.

The accurate description of a wave field is limited to the knowledge of its wave components energy, which propagates at the wave group velocity. Further, sea states that are of interest in our study, such as described by a JONSWAP wave spectrum, yield a fairly concentrated energy around their peak frequency. This allows using a finite frequency bandwidth to describe the evolution of such sea states. Hence, the intersection of the slowest and fastest wave components in the finite frequency bandwidth of the wave field determine the boundary of the spatio-temporal region within which an amount of information sufficient to issue a prediction is available. Consequently, as time increases, the accessible prediction region shrinks, to eventually disappear when the assimilated information is completely dispersed. Fig. 1 illustrates this phenomenon for a one-directional wave field propagating in the x -direction. The latest time used in data assimilation corresponds to the reconstruction time $t_r = t_{(k=K)}$. When only spatial data are used in the assimilation (i.e., $K = 1$, see Fig. 1a), the prediction zone at reconstruction time $\mathcal{P}(t_r)$ is the spatial area where observations were made. However, when spatio-temporal data sets are acquired (over an assimilation time T_a , see Fig. 1b), $\mathcal{P}(t_r)$ expands due to the advection of wave information during T_a .

Therefore, a point $(x, t \geq t_r)$ is included in the prediction zone if

$$x_b + c_{g_1}(t - t_r) \leq x \leq x_e + c_{g_2}(t - t_r), \quad (16)$$

where c_{g_1} and c_{g_2} are the fastest and slowest group velocities, respectively, and x_b and x_e define the beginning and the end of $\mathcal{P}(t_r)$ (Fig. 1) as

$$\begin{cases} x_b = \min(x_j), \\ x_e = \max(x_j) + c_{g_2} T_a, \end{cases} \quad (17)$$

where x_j are spatial locations of the observations. Although future applications could rely on observations with spatial location variations, i.e., x_j functions of time, the presented investigations are restricted to fixed measurement locations.

3.3. Bandwidths of the reconstructed wave field

As mentioned above, the accurate representation of the wave field dynamics can be ensured by selecting a finite wavenumber bandwidth having relevant cutoff limits $k^{\min, \max}$. However, the spatio-temporal characteristics of the observation grid limit the wave information that is accessible for reconstruction, thus imposing constraints on these cutoffs. For instance, the smallest wavenumber that is measurable in a given grid $k^{\min} = 2\pi/L_o$ is function of the largest distance $L_o = x_e - x_b$ between two observation points at reconstruction time t_r (Fig. 1b). At the same time, x_e is a function of the chosen minimum group velocity c_{g_2} of individual wave components in the wave field.

When reconstructing a wave field over a uniformly sampled observation grid (i.e., one with constant spatial sampling), the maximum

high cutoff wavenumber must satisfy Shannon's condition, i.e., $k^{\max} \leq 2\pi/(2\ell_o)$ where ℓ_o is the distance between two observation points. However, using an optical sensing method, the observation grid is highly non-uniform, and k^{\max} must be set such that the spectral energy truncated at higher frequencies be negligible for the dynamic description of the wave field. In later applications, we use $k^{\max} = 20k_p < \min(2\pi/(2\Delta x))$ with Δx the distance between two consecutive observation points and k_p the wavenumber of the peak spectral energy.

3.4. Group velocities for the determination of the prediction zone

In applications, the cutoff frequencies calculated as discussed above may be too restrictive to estimate the evolution of the prediction zone, i.e., due to the asymptotic behavior of the wave spectrum as the wavenumber goes to infinity, the high cutoff wavenumber tends to be larger than necessary. Instead, the group velocities $c_{g_{1,2}}$ governing the evolution of the prediction zone boundaries are defined on the basis of angular frequencies ω_1 and ω_2 corresponding to a low and high minimum energy threshold, respectively, in the wave energy density spectrum as

$$S_\eta(\omega_1) = S_\eta(\omega_2) = \mu S_\eta(\omega_p), \quad (18)$$

where $S_\eta(\omega)$ is the wave energy density spectrum, ω_p is the peak angular frequency and $\mu \ll 1$ is a small fraction of the peak spectral energy ($\mu = 0.05$ is used throughout the paper). In the following, the linear deep water dispersion relationship is used to estimate the group velocities from $\omega_{1,2}$, i.e., $c_g = g/(2\omega)$.

4. Experimental and numerical frameworks

Applications presented hereafter are based on surface elevations measured in laboratory experiments and computed in corresponding numerical simulations. Both data sets are referred to full scale wave parameters, but they are both performed at a $\ell^* = 1:50$ geometric scale (corresponding time scale is $t^* = \sqrt{\ell^*} \approx 7.06$ under Froude scaling), for long-crested wave trains generated in the oceanic 3D tank of École Centrale de Nantes (ECN), which is 50 m long, 30 m wide, and $d = 5$ m deep. Waves are generated at one side of the tank by 48 individual rotating flaps, and absorbed by a beach at the other extremity. Numerical simulations are performed using the open-source code HOS-NWT¹ developed at ECN. It makes use of the HOS method to simulate a numerical wave tank, and has been extensively used and validated against real wave tank experiments (Bonnetfoy et al., 2010; Ducroz et al., 2012). Based on a pseudo-spectral approach, the HOS method solves, to an arbitrary order M in wave steepness, the nonlinear free surface boundary conditions for a velocity potential. A converged

¹ <https://github.com/LHEEA/HOS-NWT>.

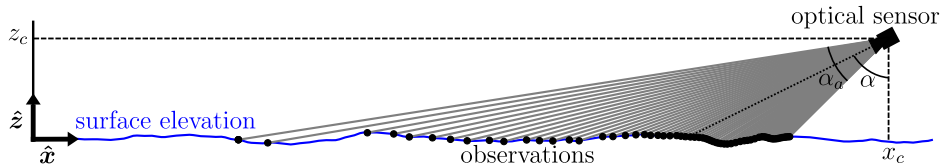


Fig. 2. Spatial sampling of a long-crested wave field by an optical sensor.

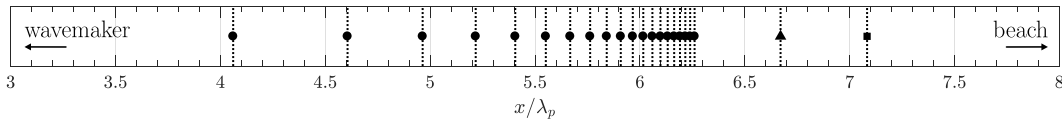


Fig. 3. Location of observation wave gauges 1 to 20 (●) and of two additional downstream gauges 21 (▲) and 22 (■). The wavemaker is located at $x/\lambda_p = 0$ and the beach at $x/\lambda_p \approx 14.86$.

estimate of the potential (for which a value of $M = 7$ is used hereafter) gives access to the fully nonlinear solution. In Section 6, this numerical model is used to improve the analysis pertaining to the experimental results. As waves of characteristic wave steepness larger than $H_s/\lambda_p \sim 0.035$ (where $\lambda_p = 2\pi/k_p$ is the peak wavelength) will start breaking, a wave breaking model allowing to both detect impending breaking and absorb wave energy is used in HOS-NWT (Seiffert et al., 2017; Seiffert and Ducrozet, 2018). The same wavemaker motion is specified in both laboratory experiments and numerical simulations, which ensures a consistent comparison between experimental and numerical results.

In the following, we first detail the experimental and numerical setups used to acquire/compute surface elevation data. An analysis of experimental measurements is then performed through the characterization of noisy perturbations. Finally, we present relevant indicators of the quality of free surface prediction and the procedure implemented to reliably evaluate them.

4.1. Description of the experimental/modeling setups

As shown in Fig. 2, spatial sampling of a free surface elevation by an optical sensor exhibits gaps due to shadowing effects from the illuminated wave fronts and, assuming a uniform distribution of beams over the sensor’s aperture angles, measurement points density geometrically decreases with the distance from the sensor.

In experiments/simulations, free surface elevations are measured/computed at 22 wave gauges (resistive probes in experiments), irregularly distributed along the wave direction of propagation. Consistent with an optical sensor facing the “wavemaker side” of the tank, the first 20 measurement points have a decreasing density away from it, corresponding to the intersection with a surface of uniformly angularly spaced beams propagating away from a point source (e.g., LIDAR camera). We consider the illumination of a flat surface, which allowed us to position the gauges vertically into the water. This way, wave-shadowing effects are not reproduced but only the geometrically decreasing density of observations, which is the prominent source of irregularity in the measurement points locations. The virtual sensor is located at an elevation $z_c = 30$ m (0.6 m in tank scale, $z_c/\lambda_p \approx 0.19$) and aimed at the water surface with an angle $\alpha = 76^\circ$ and 20 virtual beams which are uniformly spread over an aperture angle of $\alpha_a = 20^\circ$ (see Fig. 2 for a representation of α and α_a). The resulting geometrical distribution of the wave gauge locations is depicted in Fig. 3. Two additional gauges measure downstream elevations for comparison with predictions. Every gauge is labeled according to its x -location, from 1 for that closest to the wavemaker to 22 for that furthest away. Wave gauges provide observations that are used as input to the surface reconstruction and prediction algorithms. The number of spatial observations is thus constant at $J = 20$, and the number of observation times K depends on the assimilation time duration T_a and data acquisition time step τ as $K = T_a/\tau$.

Table 1

Summary of the targeted and generated full-scale sea states in both experiments and numerical simulations. Each case is labeled in alphabetical order from the smallest to the largest characteristic wave steepness H_s/λ_p .

Case	Target		Experiments		Simulations	
	H_s [m]	H_s/λ_p [%]	H_s [m]	H_s/λ_p [%]	H_s [m]	H_s/λ_p [%]
A	1.00	0.64	0.89	0.57	1.01	0.65
B	2.00	1.28	1.86	1.19	2.02	1.29
C	3.00	1.92	2.81	1.80	3.02	1.93
D	4.00	2.56	3.79	2.43	4.01	2.57
E	5.00	3.20	4.64	2.97	4.98	3.18
F	6.00	3.84	5.60	3.59	5.87	3.76
G	7.00	4.48	6.46	4.14	6.69	4.28
H	9.00	5.76	8.02	5.13	8.06	5.16

In both experiments and numerical simulations, we consider a full-scale one-directional wave field extracted from a JONSWAP spectrum with a $T_p = 10$ s peak period (≈ 1.41 s in tank scale) and a $\gamma = 3.3$ peakedness parameter. Eight sea-states were generated using the same set of wave phases (Table 1), with their significant wave height $H_s = H_{m0} = 4\sqrt{m_0}$ (where $m_0 = \int_0^{+\infty} S_\eta(f) df$) selected such that the characteristic steepness H_s/λ_p varies between $\sim 0.6\%$ and $\sim 5\%$, with $\lambda_p \approx 156$ m (3.12 m in tank scale). In tank scale we have $\lambda_p < d$, which confirms that the deep water approximation is applicable.

A theoretical wavemaker motion is deduced by applying a transfer function based on the one-directional finite-depth linear wavemaker theory and on the wavemaker geometry, which is, for both experiments and simulations, a rotating flap that is hinged three meters below the mean surface level. The amplitude of the wavemaker deflection is adjusted according to the target H_s values. Without further consideration, the obtained theoretical motion serves as input for our physical and numerical wavemakers.

We notice differences between the target and generated significant wave heights (refer to Section 4.2 for the explicit formulation Eq. 4.2 for the calculation of H_s). In experiments, H_s values are found consistently lower than target values. For sea states of small to moderate steepness (cases A to D), this is mainly explained by the wavemaker transfer function leading the physical wavemaker to generate waves of lower amplitude than according to the input. In contrast, simulations yield H_s values that are slightly higher than the targets by an amount that is of the same order of magnitude as the expected effect pertaining to the wave reflection on the beach (i.e., lower than 1%). Since the numerical beach is set such that its reflection rate corresponds to the physical one, wave reflection is expected to have a similar effect on the experimental results, i.e., very limited. For high steepness, i.e., $H_s/\lambda_p \gtrsim 3.5\%$ (cases E to H), wave breaking events appear, dissipating energy and reducing our estimates of H_s . Wave-breaking dissipation is encountered in both experiments and simulations due to the wave breaking modeling in the numerical model.

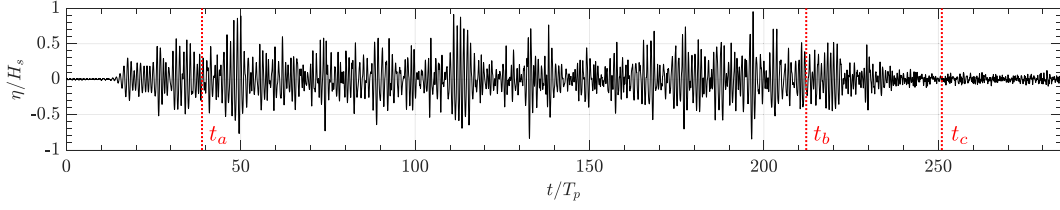


Fig. 4. Time series of surface elevation measured in experiments at gauge 22 for case E (Table 1). Three characteristic times are marked on the record, t_a : all the generated wave components have been measured at all gauges; t_b : shutdown of the wavemaker; t_c : all the generated wave components have propagated past all gauges.

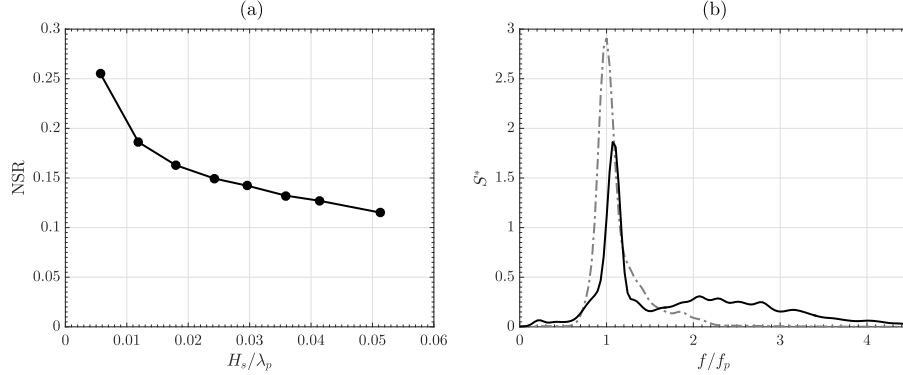


Fig. 5. (a) Noise amplitude to wave amplitude ratio as a function of characteristic wave steepness, and (b) normalized noise (—) and wave (---) spectra averaged over all the characteristic wave steepnesses.

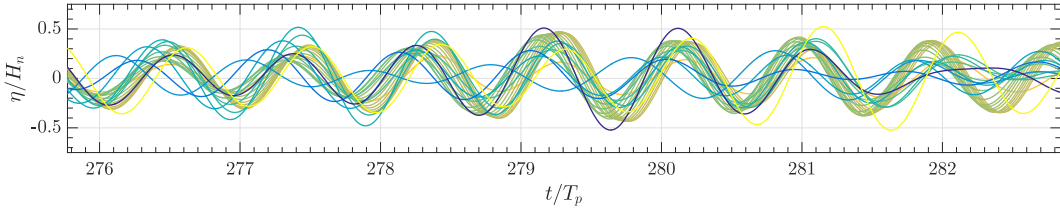


Fig. 6. Normalized surface elevations for case A at the locations of gauges 1 to 22. Components of frequency higher than $1.4f_p$ has been removed using a low-pass filter.

4.2. Analysis of experimental data

Fig. 4 shows a typical time series of surface elevation measured at a resistive probe in laboratory experiments. Time $t = 0$ corresponds to the start of the wavemaker motion, i.e., the beginning of wave generation. At time t_a , it is estimated based on a truncation of the prescribed wave energy spectrum (similar to Section 3.4) that all the energetic wave components generated at the wavemaker have been seen by all gauges. At time t_b , the wavemaker is shutdown and waves generation is interrupted. Finally, similar to the determination of t_a , at time t_c , it is estimated that all the generated energetic wave components have propagated past all gauges. Based on this, the data used for the wave field prediction study is restricted to the time interval $[t_a, t_b]$, with $t_b - t_a \approx 173T_p$.

It is desirable to analyze and quantify the influence of the perturbations pertaining to the limitations of our experimental setup (referred to as “noise” throughout this work) on the recorded wave signal. This is done by considering that the rest of the data acquired at wave gauges, for a few dozen peak wave periods beyond $t = t_c$, provides a representation of noise during the entire data acquisition duration. Based on this data, a noise to signal ratio $\text{NSR} = H_n/H_s$ is computed as a function of characteristic heights for both the primary wave ($t \in [t_a, t_b]$) and noise ($t \geq t_c$) signals following

$$\begin{cases} H_s = \frac{1}{N_p} \sum_{j=1}^{N_p} 4 \sigma_\eta(x_j, t_a \leq t \leq t_b), & \text{(a)} \\ H_n = \frac{1}{N_p} \sum_{j=1}^{N_p} 4 \sigma_\eta(x_j, t \geq t_c), & \text{(b)} \end{cases} \quad (19)$$

respectively, where $\sigma_\eta(x, t)$ denotes the standard deviation of the free surface elevation $\eta(x, t)$ and $N_p = 22$ wave gauges. The NSR is computed for each case A to H in Table 1 and plotted in Fig. 5a as a function of the corresponding characteristic wave steepness. We see that the NSR decreases as a function of wave steepness, with the largest value being about 25% for the smallest steepness and the smallest value being about 11.5% for the largest steepness. It thus appears that the geometry of our experimental set-up, in a 3D wave tank allowing the generation of directional wave fields, may have significantly affected the targeted one-directional wave fields. As will be detailed in Section 6.3, this potentially large NSR may affect the performance of the wave prediction algorithm.

To better quantify noise effects on the desired experimental data and relate the generated noise to a physical process, we computed the power spectral density S_n of the noisy part of the signal ($t \geq t_c$). For each steepness, the spectrum was averaged over results obtained at the 22 wave gauges and normalized as $S_n^* = S_n f_p / m_0$, where $m_0 = H_n^2 / 16$ is the zeroth-order moment of the spectrum. These normalized noise spectra were found to be nearly identical for each steepness. Fig. 5b shows their average, which is composed of a narrow-banded peak, centered on $\sim 1.1f_p$, and a broad-banded high frequency part of much lower amplitude. The wave spectrum, calculated on $[t_a, t_b]$, is given on the same figure as a visual help for interpretation. Fig. 6 shows normalized surface elevations of the noise signal η/H_n in which frequencies $f > 1.4f_p$ have been removed by filtering, i.e., these correspond to the dominant part of the noise signal. It shows that

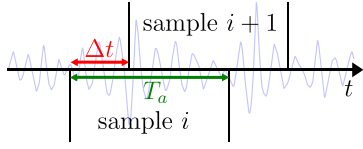


Fig. 7. Each sample consists of a time trace from the same generated surface realization. They can be partially overlapping, separated by a time span Δt from their neighbors.

elevations for case A at wave gauges 1 to 22 (which are aligned along the x -direction) are mostly in phase, suggesting that the dominant experimental noise may be caused by resonant excitations of transverse modes in the 3D wave tank. This hypothesis is confirmed by our visual observations of these waves during calm-down times between measurements, and is explained by the presence of small interstices between the wavemaker flaps, locally generating transverse disturbances. The much less energetic noisy components of the signal, with frequencies $f > 1.4f_p$, were not found to be in phase, indicating that they result from aleatory processes.

4.3. Misfit indicators definitions

The misfit indicator used to quantify the accuracy of the predicted wave field is defined as

$$\mathcal{E}(x, t) = \frac{1}{N_s} \sum_{i=1}^{N_s} |\eta_i(x, t) - \eta_{ri}(x, t)| / H_s, \quad (20)$$

where η is the predicted surface elevation and η_r is the reference surface (measured or calculated, depending on whether experimental or numerical data is used). To better assess its overall behavior, the misfit is averaged over N_s surface samples, denoted by index i . An unbiased estimate can only be obtained for a large number of samples from independent wave field realizations (i.e., of different sets of random wave phases) with, to the limit, $N_s \rightarrow \infty$. Instead, we elected to generate one single surface realization per sea state, but to record or compute wave gauge data over a long time so that the signals can be split into a sufficiently large number of samples of meaningful duration T_a . Additionally, the number of samples is increased by selecting them as partially overlapping, i.e., shifting them in time by $\Delta t < T_a$, as illustrated in Fig. 7. Therefore, the information used to estimate the misfit is the surface elevation data in the total time window covered by the samples, which has a duration $T_c = T_a + (N_s - 1) \Delta t$. A similar approach was employed in Naaijen et al. (2014) to investigate the spatio-temporal evolution of the prediction zone based on experimental and numerical data. The wave field prediction error at a specific location x is finally computed by averaging the corresponding misfit over the theoretical time-prediction zone $t \in [t^{\min}, t^{\max}]$ as

$$\mathcal{E}^{\mathcal{P}}(x) = \frac{1}{t^{\max} - t^{\min}} \int_{t^{\min}}^{t^{\max}} \mathcal{E}(x, t) dt. \quad (21)$$

Fig. 8 shows, for case E, the evolution of the wave field prediction error $\mathcal{E}^{\mathcal{P}}$ computed as a function of the amount of data used to calculate it, quantified by the relative duration T_c/T_p of the time window used to evaluate the misfit \mathcal{E} . We see that the prediction error converges for $T_c/T_p \sim 60$. Note that the wave gauge network used to generate the observations covers a zone only slightly larger than $2\lambda_p$. If this zone was larger, the optimal number of peak wave periods for the sampling time window would likely be less than 60.

Additionally, for deterministic comparison, we make use of the cross-correlation between time series corresponding to the predicted and the measured surface elevations, which provides a correlation factor C as a function of a time-lag \mathcal{T} . The maximal value of the correlation factor and its corresponding time-lag can be interpreted as the correspondence in terms of shape and amplitude of the two

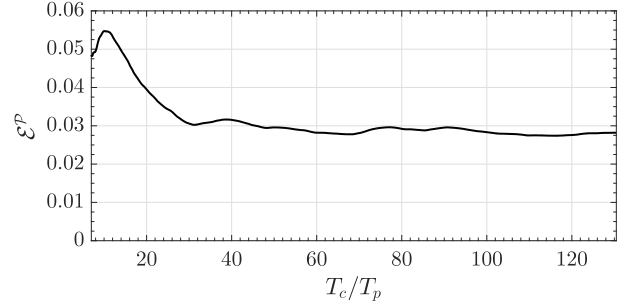


Fig. 8. Nonlinear (ICWM) prediction error estimate at the location of gauge 22 as a function of the length of the time window used to evaluate the misfit, $T_c = T_a + (N_s - 1) \Delta t$, normalized by the peak spectral period T_p , and in which $\Delta t/T_p \approx 0.07$. Here, $T_a/T_p \approx 7$ and $\tau/T_p \approx 0.07$, and simulated reference data from case E are used.

elevations, and as an estimate of the time shift between the two elevations, respectively. The cross-correlation is defined by

$$C(\mathcal{T}) = \frac{1}{t^{\max} - t^{\min}} \int_{t^{\min}}^{t^{\max}} \eta^*(t) \times \eta_r^*(t + \mathcal{T}) dt, \quad (22)$$

where $t^{\min, \max}$ are the prediction zone boundaries and $\eta^*(t) = \eta(t) / \sigma_\eta$ ($t^{\min} \leq t \leq t^{\max}$) is the normalized free surface elevation (similarly, $\eta_r^* = \eta_r / \sigma_{\eta_r}$ for the reference surface).

5. Prediction error sensitivity to reconstruction algorithm

We first assess the sensitivity of the prediction error to both the method used (linear or nonlinear) and parameters of the assimilation procedure, namely the assimilation time T_a and the time shift of the assimilated data τ .

For case A, which corresponds to a mild characteristic wave steepness of 0.65%, Fig. 9a shows that the linear prediction error converges well as T_a increases, for the three considered τ values, although convergence is slower for larger τ . Hence, the converged error is independent of the time resolution of observations. This is a consequence of the characteristics of the physical description emerging from observations. As the assimilation time increases, the diversity of wave processes included in the assimilated information is enhanced, with respect to the relevant physics simulated in the model, causing the prediction error to converge. Additionally, the accuracy of the description of physical phenomena, which is directly function of the time resolution of observations, affects the prediction error convergence rate: for a given assimilation time T_a , a smaller time step τ will yield a prediction error closer to the converged value. For the predictions presented later, we keep $\tau/T_p \approx 0.07$.

For case E, which corresponds to a larger wave steepness of 3.18% and hence a fairly nonlinear case, Fig. 9b shows that, overall, prediction errors are larger than for case A, increasing from [0.005, 0.05] to [0.05, 0.075]. Fig. 9b also shows that, as could be expected for this nonlinear case, the prediction errors are larger with the linear method than with the nonlinear method. Finally, the convergence of the nonlinear method to achieve an approximately constant value of $\mathcal{E}^{\mathcal{P}}$ requires a slightly larger T_a than for the linear method. This can be explained by the higher level of physics represented in the ICWM model than in LWT, which requires larger time scales to achieve convergence.

6. Prediction results and discussion

Applications of the reconstruction and forecasting algorithms to cases of Table 1 are presented in the following and the accuracy of the wave field forecast is discussed, in particular, in terms of its sensitivity to the linear or nonlinear methods used.

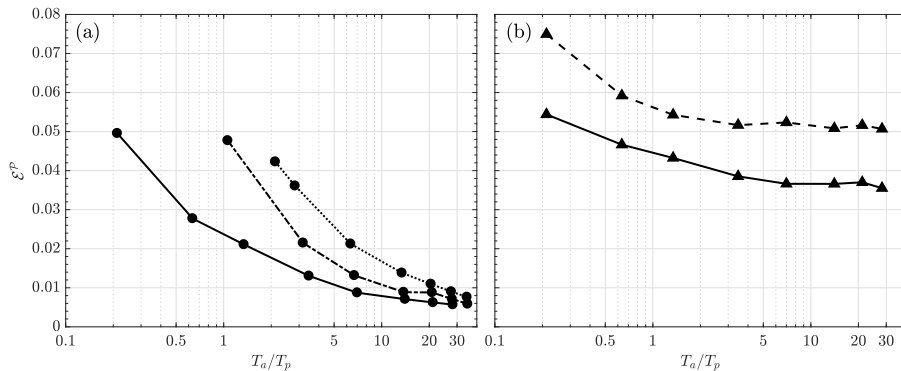


Fig. 9. Prediction error at the location of gauge 22 as a function of the normalized assimilation time T_a/T_p in case (a) A (●) and (b) E (▲). In case A, the linear error is plotted for $\tau/T_p \approx 0.07$ (—), 0.35 (---) and 0.71 (·····). In case E, a time step $\tau/T_p \approx 0.07$ is used and both the linear (LWT, ---) and nonlinear (ICWM, —) errors are plotted. Simulated reference data is used in both figures.

6.1. Wave group analysis

All cases in Table 1 correspond to sea states generated using a JONSWAP spectrum with identical peak period $T_p = 10$ s (at full scale) and peakedness $\gamma = 3.3$, but a different significant wave height H_s and, hence, characteristic wave steepness H_s/λ_p . In both the physical and numerical wave tanks, these sea states are generated using the same set of random phases, so time series of surface elevations should be similar, except for small changes in amplitude due to nonlinear effects, proportional to H_s .

In the following, we analyze the prediction error for a group of 8 waves of elevation on the order of $\eta \sim 0.5H_s$ approximately centered at $t = 113T_p$, recorded/simulated at wave gauge 22 for cases A to H (see Fig. 4). The data used in the prediction algorithms was selected for the prediction zone to span $t \approx 108T_p$ to $118T_p$ at the location of gauge 22. Fig. 10 shows time series of surface elevations for these wave groups in cases A, E and H, compared to predictions of the linear (LWT), linear corrected (LWT-CDR), and nonlinear (ICWM) models, using experimental (a, c, e) and numerical (b, d, f) data. For each case, only small differences due to experimental noise can be seen between the experimentally and numerically generated reference surfaces. While there is an overall agreement between the reference and predicted surfaces, differences in wave phase and elevation increase with wave steepness, due to cumulative effects of nonlinearity during wave propagation. Accordingly, for the smallest wave steepness (case A), all three models predict the same surface elevation, in good agreement with references, particularly for numerical data (b) for which predictions almost perfectly overlap the HOS solution, but predictions become increasingly different between the three algorithms, the larger the characteristic wave steepness. Although differences do not appear visually large, this is more pronounced for the algorithm based on ICWM, which, as will be shown next using various prediction error metrics, provides the most accurate prediction.

Differences between the reference (measured or simulated with HOS) surface elevations and those predicted by the three algorithms are quantified by their maximum cross-correlation $\max(C)$ (i.e., normalized convolution, Eq. (22)) and corresponding time-lag $\mathcal{T}_s = \arg \max(C)$. Both parameters are shown in Fig. 11 for all cases in Table 1, based on time series measured or simulated at the location of wave gauge 22 (e.g., Fig. 10). The former quantifies the accuracy of the prediction in terms of wave shape and amplitude, while the latter quantifies the time-shift of the predicted signal compared to the reference signal. Fig. 11a, b show that, for all prediction algorithms, time-lag increases with wave steepness (i.e., nonlinearity), from 0 for the smallest steepness to a few percent of T_p for the largest one, consistent with the expected effects of nonlinearity. As seen for instance in the time series of Fig. 10, LWT yields the largest time-lags compared to the nonlinear models.

LWT-CDR, which includes a phase shift correction, provides a time-lag very close to that of ICWM, particularly for the simulated data, indicating that the nonlinear phase shift prevails over the nonlinear wave geometry represented in the latter model for these cases. Also, the rate of increase of time-lag with wave steepness is similar whether or not the nonlinear phase shift is included in the model. This result is unexpected since this phase shift is due to nonlinear amplitude dispersion, which is function of wave steepness.

Fig. 11c, d show the maximum cross-correlations for the same cases. Consistent with the larger time-lag, $\max(C)$ mostly decreases, the larger the wave steepness, to reach a minimum of 96% for the largest wave steepness. Except for case G, which is discussed below, the maximum cross-correlation is larger using ICWM, which is expected since only this model is able to represent nonlinear wave geometry. The abnormal behavior of case G, which is seen in both the experimental and numerical data, likely results from a significant increase in wave breaking events within the considered wave group for this case. Note, for case H, which has an even larger steepness, wave phases were such that breaking was not as widespread as for case G. Wave breaking affects wave geometry in a non-trivial manner and is not represented in ICWM. In the case of the wave group considered here, for some unknown reason, it appears that broken waves are better represented in the linear model than using ICWM.

Finally, Fig. 12 shows results similar to Fig. 11, using ICWM for numerical or experimental data, at wave gauges 20, 21 and 22. Observations are acquired (and reconstructed) at wave gauge 20, which is the last gauge used in observations, and predictions are made at the other 2 gauges, which are increasingly distant from it (Fig. 3). For both the experimental and numerical data, the time-lags and their rates of increase with wave steepness are lower for prediction locations closer to the observation gauge (Fig. 12a, b). This results from inaccuracies in nonlinear wave propagation modeled by ICWM, which yield increasing differences in predicted surface elevations with time or space traveled, compared to the reference data. Consistent with this observation, Fig. 12c, d show that, for steepnesses larger than $\sim 2.5\%$, the maximum cross-correlation decreases as the distance of the prediction gauge to the observation location increases.

6.2. Instantaneous misfit of wave prediction

We investigate next the evolution of the instantaneous misfit $\mathcal{E}(x, t)$ of the wave prediction for case E, which corresponds to a moderate steepness, although nonlinear effects already have a marked influence on the wave field dynamics. For both experimental and numerical cases, we compare the misfit obtained using the LWT, LWT-CDR and ICWM prediction algorithms.

Fig. 13 shows the temporal evolution of the wave prediction misfit computed using different algorithms, with respect to data simulated

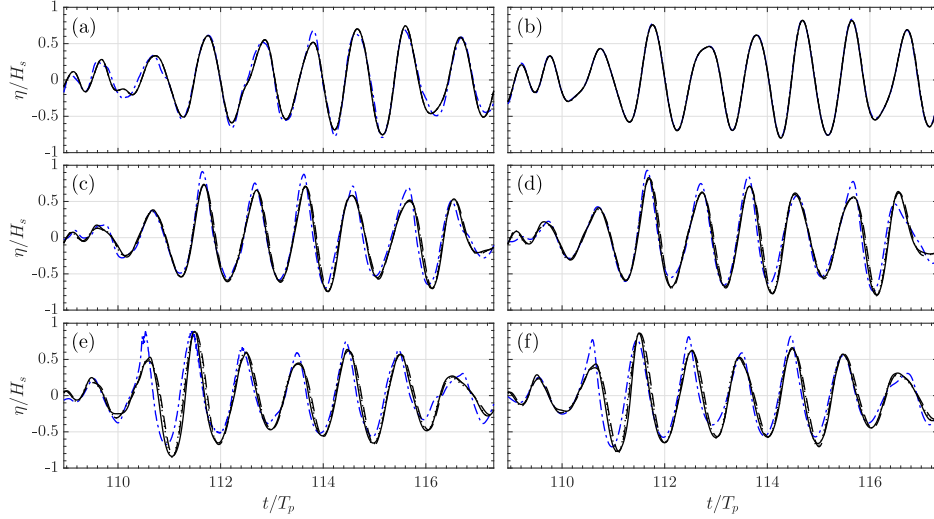


Fig. 10. Time series of surface elevations measured/simulated at gauge 22 for a group of 8 waves (---) for cases: (a, b) A, (c, d) E and (e, f) H, of increasing nonlinearity. Predicted surface elevations are shown for the: linear (LWT, - - -), corrected linear (LWT-CDR, ·····), and nonlinear (ICWM, —) models. Left (a, c, e): experiments; right (b, d, f): simulations.

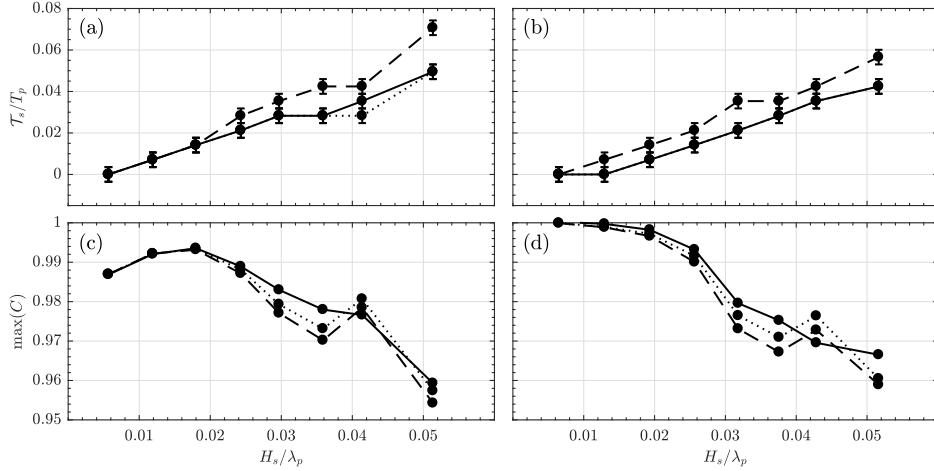


Fig. 11. Normalized time-lag (a, b) and maximum cross-correlation (c, d) computed for cases in Table 1, based on reference time series measured (left column)/simulated with HOS (right column) at the location of wave gauge 22 for wave groups similar to those in Fig. 10, based on: linear (LWT, - - -), corrected linear (LWT-CDR, ·····), and nonlinear (ICWM, —) prediction algorithms. Error bars in (a, b) result from the resolution of the time series..

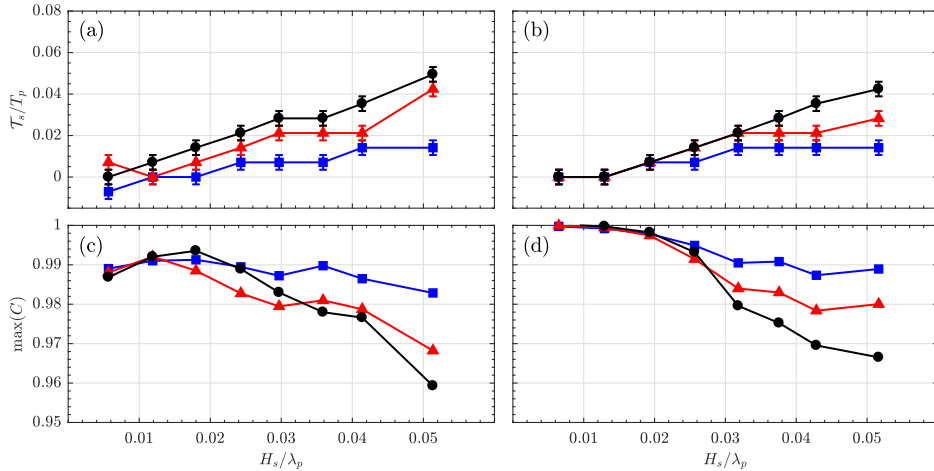


Fig. 12. Normalized time-lag (a, b) and maximum of cross-correlation (c, d) for the nonlinear (ICWM) predictions, at the location of gauge 20 (■), 21 (▲) and 22 (●). Left (a, c): experiments; right (b, d): simulations. Error bars on (a, b) correspond to the time resolution of the time series.

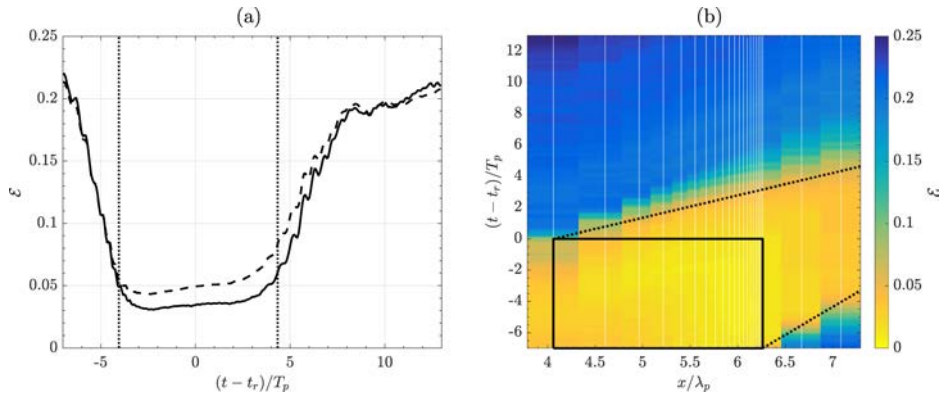


Fig. 13. Time evolution of wave prediction misfit \mathcal{E} , computed with respect to data simulated for case E: (a) at gauge 22 using the linear (LWT, - - -) and nonlinear (ICWM, —) prediction algorithms; (b) for all gauges using the nonlinear (ICWM) prediction algorithm (black rectangle encompasses assimilated observations; data was collected at gauges' x -locations (vertical lines) and interpolated using the nearest neighbor method). In each subfigure, dotted lines (.....) mark the prediction zone boundaries.

for case E, at both gauge 22 (a) and for all gauges (b). The misfit at gauge 22 is significantly lower within the accessible prediction zone, $[t^{\min}, t^{\max}]$ (Fig. 13a), reaching a minimum value of about 3.5% for ICWM, compared to about 4.5% for LWT, whose misfit is consistently about 30% larger than that of ICWM. Within the time prediction zone, the error gradually slightly increases due to the limited physics represented in both wave models. In the spatio-temporal domain (Fig. 13b), ICWM's misfit is lowest within the theoretical prediction zone, reaching a maximum of about 7% along its boundary. As the x -location of the wave gauge increases, the misfit gradient decreases across the prediction zone upper boundary t^{\max} , or in other words the transition of the misfit values from within to outside the prediction zone becomes more diffused, which is due to the dispersion of the assimilated information. More specifically, as detailed in Section 3.2, the energy associated with the reconstructed wave components disperses as x increases, gradually limiting the physical description of the wave field. Even within the spatio-temporal region corresponding to the observations (black rectangle in Fig. 13b), the misfit is non-zero since observations are discrete rather than continuous samples of elevations. Hence, the reconstructed elevation (nowcast) is always an estimate of the reference solution. Note that the accessible prediction horizon in the depicted configuration is $t^{\max} - t_r \approx 3.7T_p$ and $4.3T_p$ at gauges 21 and 22, respectively, and is expected to further increase at larger distances (at the expense of the prediction accuracy). Then, from the location where the beginning of the prediction zone t^{\min} matches the reconstruction time t_r , the accessible horizon starts decreasing.

For the same case E, Fig. 14 shows for both experimental or simulated reference data, the spatio-temporal evolution of the ratio of the nonlinear (ICWM) to linear (LWT; a, b) or linear with corrected dispersion (LWT-CDR; c, d) wave prediction misfit. For the simulated data (Fig. 14b), the misfit is reduced by up to $\sim 35\%$ within the prediction zone when using ICWM instead of LWT. Compared to LWT-CDR (Fig. 14d), the reduction is smaller and mostly limited to the spatio-temporal region of assimilated data (within the solid box), particularly where the wave gauge density is larger. Outside of this region ($t > T_a \approx 7T_p$; time propagation) or at the location of gauges 21 and 22 (space propagation), the misfit ratio rapidly approaches one, indicating that the improvement achieved using ICWM rather than LWT-CDR becomes negligible. For the experimental data (Fig. 14a, c), similar patterns are observed, but the improvement achieved using ICWM is not as pronounced as for simulated data.

These results indicate that the improved representation of nonlinear wave geometry using ICWM mostly affects the accuracy of the reconstructed part of the wave field. Once reconstructed waves are propagated to the prediction zone, the nonlinear phase shift, which is corrected in LWT-CDR to the same level as in ICWM, becomes the main source of error and effects of nonlinear wave geometry become

negligible compared to it. The wave models are parameterized to provide a relevant and consistent approximation of the wave field over the entire region covered by the observations. Hence, while the reconstructed wave field is constrained to fit the measurements, when waves are propagated to issue a prediction, only their propagation properties featured in the models come into play.

6.3. Influence of experimental noise on wave prediction

The prediction misfits based on numerical and experimental reference data are compared in Fig. 15, at gauges 20, 21, and 22, for all cases listed in Table 1, using the linear (LWT) or nonlinear (ICWM) algorithms. To better assess the effect of experimental noise on the prediction misfit, a “noisy numerical dataset” was created by adding to the numerical data a noise signal having the same spectral shape (or NSR) as that analyzed for the experiments (Fig. 5b), scaled by the measured noise amplitude H_n (Fig. 5a), with independent random phases for each wave gauge. As would be expected, for both algorithms, the prediction misfits are larger at all wave gauges using experimental data, as compared to noise-free numerical data, particularly for cases with a lower steepness, which have relatively larger noise levels. Using the noisy numerical data, however, prediction misfits increase to nearly match those of the experimental data. This indicates that the noisy numerical data is consistent with the experimental data and provides a *digital twin* of experiments that explains, for the most part, differences observed between predictions issued for experimental and noise-free numerical data.

6.4. Application to remote sensing: free surface slope prediction

In the free surface elevation predictions described above, the nonlinear phase correction was responsible for the main relative improvement in prediction misfit, rather than the nonlinear wave geometry represented in ICWM. While for many ocean engineering applications predicting instantaneous free surface elevations is most important, such as when computing wave forces or runup on structures, or controlling a wave energy converter, in some applications such as remote sensing the main parameter of interest is free surface slope, which governs the backscattered signal to the radar or optical sensor used (e.g., Noguier et al., 2010, 2014). Hence, in the following, we quantify the improvement in free surface slopes representation achieved using ICWM rather than LWT-CDR. More specifically, at the location of wave gauge 20, we analyze the evolution as a function of wave steepness of the maximum prediction misfit ratio $\mathcal{E}_{ICWM}^P / \mathcal{E}_{LWT-CDR}^P$, for both surface elevation and slope. As the distance between gauges 19 and 20

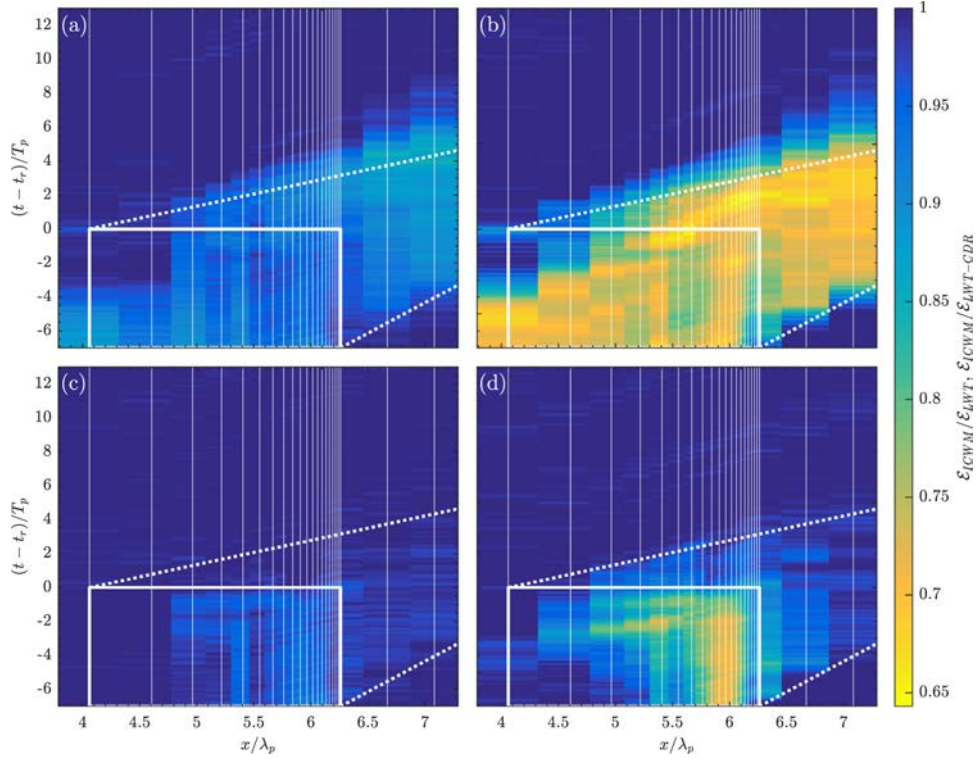


Fig. 14. Spatio-temporal evolution of the ratio of the nonlinear (ICWM) to (a, b) linear (LWT) and (c, d) linear with corrected dispersion relation (LWT-CDR) wave prediction misfit ε , with respect to: (a, c) experimental; and (b, d) simulated reference data for case E. Lines denote prediction zone boundaries (.....) and domain of assimilated data (—). Data was collected at gauges' x -locations (vertical lines) and interpolated using the nearest neighbor method.

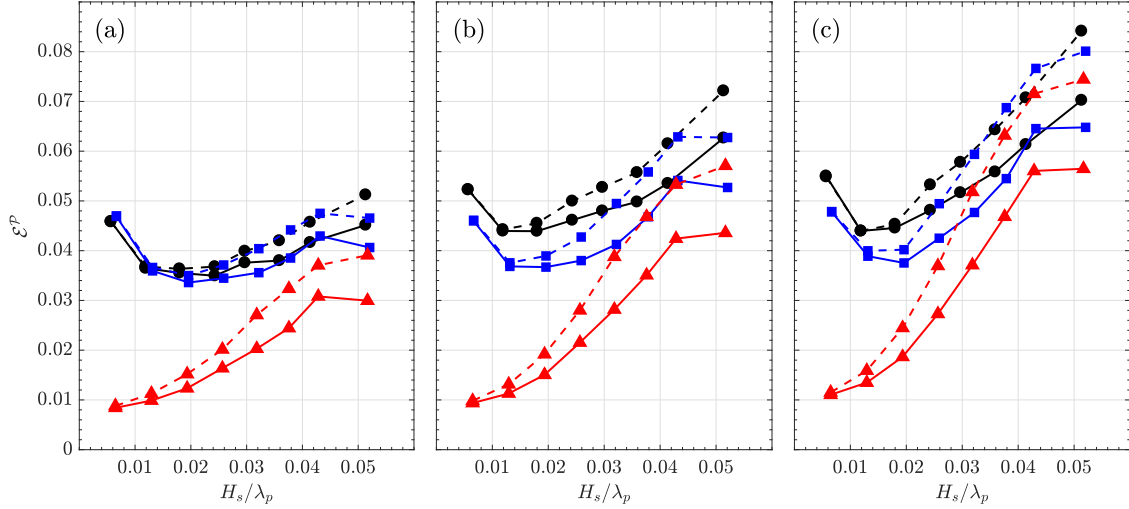


Fig. 15. Prediction misfits for all cases in Table 1, using the linear (LWT, - - -) and nonlinear (ICWM, —) algorithms, based on: experimental (●), numerical (▲), and noisy numerical (■) reference data, at gauges (a) 20, (b) 21 and (c) 22.

is small ($\sim 0.02\lambda_p$), the wave surface slope can be approximated by

$$s(t) = \frac{\eta(x_{20}, t) - \eta(x_{19}, t)}{x_{20} - x_{19}}, \quad (23)$$

where η denotes the reference or predicted surface elevation and $x_{19,20}$ the location of gauge 19 and 20. We calculate the slope prediction misfit by replacing η with s in Eq. (20).

Results in Fig. 16 show a consistently lower misfit ratio for the slope prediction, whether experimental or numerical data is used (although in the latter case the ratios are lower in absolute value), indicating that, unlike with surface elevation predictions, geometrical nonlinearities

included in ICWM provide a significant improvement for predicting surface slopes.

Further, in ICWM, geometrical nonlinearities are second-order in wave steepness whereas nonlinear phase shifts are third-order (Nouguier et al., 2009, 2010; Guérin et al., 2019). Accordingly, in Fig. 16, the improved performance of ICWM for predicting surface slopes is much more significant at small wave steepness, when third-order effects are not prominent yet. Additionally, when using numerical data, the misfit ratios for surface elevation and slope predictions become increasingly close, the larger the wave steepness. With experimental data, the residual noise causes higher-frequency surface

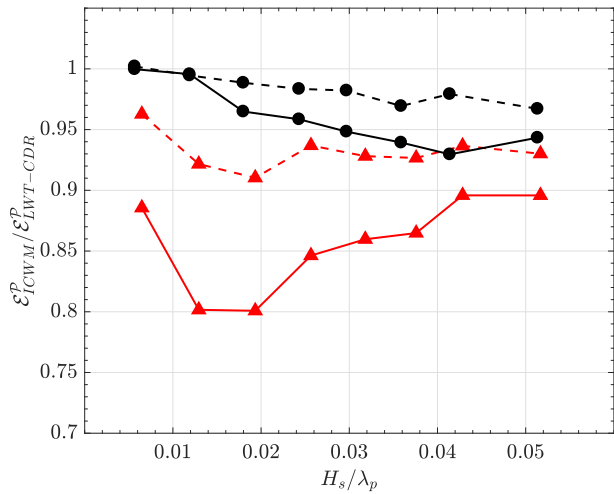


Fig. 16. Ratio of the nonlinear (ICWM) to the linear with corrected dispersion relation (LWT-CDR) prediction misfit for the surface elevation (---) and the surface slope (—) at the location of gauge 20 using experimental (●) and numerical (▲) reference data.

oscillations that significantly affect the slope calculation and prevent a proper evaluation of the corresponding prediction misfit. Hence, in Fig. 16 both elevation and slope misfit ratios are close to one at low wave steepness.

When initializing a nonlinear model based on a superposition of harmonics linearly extracted from a standard wave spectrum (such as here a JONSWAP), nonlinearity in the model equations will cause the generation of higher-frequency wave components that will translate into additional spectral energy at those frequencies from the onset. Likewise, waves generated in a wave tank based on a similar standard spectrum will evolve nonlinearly, which results in energy transfer towards higher frequencies. This energy redistribution in wave spectra is referred to as the *dressing process* (Nouguier et al., 2009). In our applications, it is thus the dressed spectrum that is calculated based on the reference surface, both in experiments and simulations. This is illustrated in Fig. 17, which shows the normalized energy density spectra of the free surface, $S_\eta^* = S_\eta f_p / (H_s^2/16)$, computed for case E over the time interval corresponding to the prediction zone $[t^{\min}, t^{\max}]$ at the location of gauge 20. Waves are only generated by both experimental and numerical wavemakers in the frequency range $f \in$

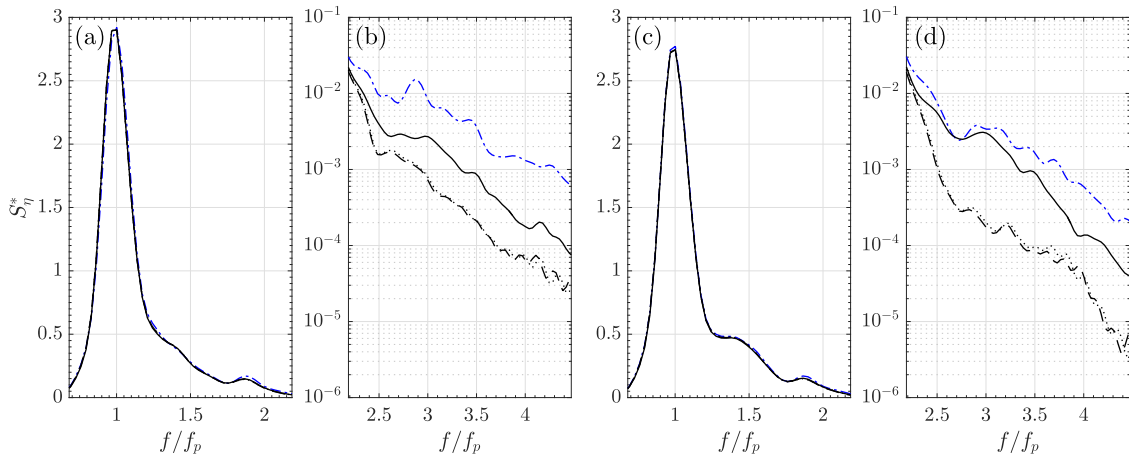


Fig. 17. Normalized energy density spectra of free surface elevations computed for case E over $t \in [t^{\min}, t^{\max}]$, at gauge 20, for the: reference data (---), ICWM model (—), LWT model (---) and LWT-CDR model (·····), in: (a, b) experiments; (c, d) simulations.

$[f_l, f_h]$, with $f_l \approx 0.68f_p$ and $f_h \approx 2.18f_p$, the low and high cut-off frequencies, respectively. Within this frequency range (Fig. 17a, c), spectral amplitudes agree well with each other for the reference data and all wave models. However, as a result of nonlinearity in the reference data, for $f > f_h$ (Fig. 17b, d), energy increases in all cases as compared to the targeted spectrum. More specifically, while for $f > f_h$ spectral amplitudes are lower in all the models than in the reference data, ICWM provides results in much better agreement with the latter, particularly for the numerical reference data, and LWT and LWT-CDR provide similar results, both lower than those of ICWM. These results confirm that high-frequency wave components that predominantly affect wave slope predictions, are more accurately predicted with the latter model, due to its representation of nonlinear wave geometry (e.g., sharper crests).

7. Conclusions

In the context of the deterministic prediction of ocean surface waves, we assessed and compared the accuracy of three ocean wave prediction algorithms, based on three wave models having different nonlinear properties. The algorithms were tested against data (time series of surface elevation) acquired for long-crested wave fields using wave gauges, in wave tank experiments as well as in simulations of similar experiments with a high-order numerical wave tank. A number of test cases were defined with different characteristic wave steepness, from mildly to more strongly nonlinear. The set of wave gauges (physical or numerical) was non-uniformly distributed in space, to mimic the typical uneven sampling made by optical sensors at grazing incidence. The wave models used in the prediction algorithms were inverted based on the wave gauge data and reconstructed waves were then propagated with the models. Residual oscillations observed in the physical wave tank were investigated and found to result from perturbations caused by the wavemaker. These oscillations were identified as the principal cause for observed differences between the experimental and numerical data. Adding the experimental noise to numerical reference data in fact led to similar levels of wave prediction misfit (or accuracy) as when using experimental data.

Our study showed that the prediction accuracy of the algorithms, quantified by a misfit parameter, converged with the duration of the assimilated surface elevation time series (i.e., amount of data used). In addition, smaller data acquisition time steps yielded higher convergence rates, and the larger the characteristic wave steepness, the larger the prediction error, in the form of nonlinear phase shifts (related to wave phase velocity) and wave shape discrepancies. The recently developed Improved Choppy Wave Model (ICWM, introduced in Guérin

et al., 2019) yielded improved predictions within the accessible prediction zone, as compared to a linear wave model, with a maximum prediction misfit reduction of $\sim 35\%$ for an intermediate wave steepness, $H_s/\lambda_p \approx 3.18\%$ (based on numerical data). In the spatio-temporal region corresponding to the observations, the wave shape asymmetry represented in ICWM improved the surface elevation representation. For waves that had propagated (in space and/or time), the main factor for reducing the prediction misfit was the accurate modeling of nonlinear wave phase velocity. For surface slope predictions, however, the improved representation of wave shape asymmetry in ICWM allowed to achieve an average prediction misfit reduction of 20% over the prediction zone, for a low wave steepness of $\sim 1\text{--}2\%$, as compared to a linear model with a phase speed correction (LWT-CDR). Note that higher-order wave models (e.g., HOS, MNLS) are expected to further improve the prediction accuracy, but only provided that the assimilation procedure yields the correct initial model parameters, which becomes increasingly complex and time-consuming when the model order increases. Using such models to propagate waves will also require a much larger computational effort.

Lessons learned in this study will help applying our prediction algorithms to data acquired at sea using optical sensor systems, such as LIDARs (e.g., Belmont et al., 2007; Noguier et al., 2014). As the method described here is directly applicable for predicting directional wave fields, further investigation of the performance of our algorithms for short-crested waves will be pursued in future work.

CRediT authorship contribution statement

N. Desmars: Conceptualization, Methodology, Software, Validation, Formal analysis, Investigation, Data curation, Writing - original draft, Writing - review & editing, Visualization. **F. Bonnefoy:** Conceptualization, Methodology, Validation, Formal analysis, Investigation, Data curation, Writing - review & editing. **S.T. Grilli:** Conceptualization, Validation, Writing - review & editing. **G. Ducrozet:** Conceptualization, Methodology, Validation, Writing - review & editing, Supervision. **Y. Perignon:** Conceptualization, Methodology, Validation, Investigation, Data curation, Writing - review & editing, Supervision, Project administration, Funding acquisition. **C.-A. Guérin:** Conceptualization, Methodology, Validation, Writing - review & editing. **P. Ferrant:** Conceptualization, Validation, Writing - review & editing, Supervision.

Declaration of competing interest

The authors declare that they have no known competing financial interests or personal relationships that could have appeared to influence the work reported in this paper.

Acknowledgments

This work was supported by Naval Group and École Centrale de Nantes (ECN) through their Joint Laboratory for Marine Technology, and by the PREDEMO-NAV project grant ANR-15-ASTR-0006, of the French Agency for National Research. SG also acknowledges support from the US National Science Foundation, Physical Oceanography Program grant OCE-1947960 to the University of Rhode Island. The ECN ocean tank staff is gratefully acknowledged for its support in the experimental part of this work. The authors would also like to thank the reviewers for their constructive comments and suggestions to improve the initial manuscript.

References

Belmont, M.R., Horwood, J.M.K., Thurley, R.W.F., Baker, J., 2007. Shallow angle wave profiling lidar. *J. Atmos. Ocean. Technol.* 24 (6), 1150–1156, URL <https://doi.org/10.1175/JTECH2032.1>.

Blondel, E., 2009. Reconstruction et prévision déterministe de houle à partir de données mesurées (Ph.D. thesis). École Centrale de Nantes, URL <https://tel.archives-ouvertes.fr/tel-00449343>.

Blondel, E., Bonnefoy, F., Ferrant, P., 2010. Deterministic non-linear wave prediction using probe data. *Ocean Eng.* 37 (10), 913–926, URL <http://www.sciencedirect.com/science/article/pii/S0029801810000661>.

Bonnefoy, F., Ducrozet, G., Le Touzé, D., Ferrant, P., 2010. Advances in Numerical Simulation of Nonlinear Water Waves. *World Scientific*, pp. 129–164, Ch. Time-Domain Simulation of Nonlinear Water Waves Using Spectral Methods. URL https://www.worldscientific.com/doi/abs/10.1142/9789812836502_0004.

Calvetti, D., Reichel, L., Shuibi, A., 2004. L-curve and curvature bounds for Tikhonov regularization. *Numer. Algorithms* 35 (2–4), 301–314, URL <https://doi.org/10.1023/B:NUMA.0000021764.16526.47>.

Desmars, N., Perignon, Y., Ducrozet, G., Guérin, C.-A., Grilli, S.T., Ferrant, P., 2018. Phase-resolved reconstruction algorithm and deterministic prediction of nonlinear ocean waves from spatio-temporal optical measurements. In: *International Conference on Offshore Mechanics and Arctic Engineering*, Volume 7B: Ocean Engineering. pp. 1–12, V07BT06A054. URL <https://doi.org/10.1115/OMAE2018-78367>.

Ducrozet, G., Bonnefoy, F., Le Touzé, D., Ferrant, P., 2012. A modified High-Order Spectral method for wavemaker modeling in a numerical wave tank. *Eur. J. Mech. B/Fluids* 34, 19–34, URL <http://www.sciencedirect.com/science/article/pii/S0997754612000180>.

Fujimoto, W., Waseda, T., 2020. Ensemble-based variational method for nonlinear inversion of surface gravity waves. *J. Atmos. Ocean. Technol.* 37 (1), 17–31, URL <https://doi.org/10.1175/JTECH-D-19-0072.1>.

Gerstner, F., 1809. Theorie der Wellen. *Ann. Phys.* 32 (8), 412–445, URL <https://onlinelibrary.wiley.com/doi/abs/10.1002/andp.18090320808>.

Grilli, S.T., Guérin, C.-A., Goldstein, B., 2011. Ocean wave reconstruction algorithms based on spatio-temporal data acquired by a flash LIDAR camera. In: *Proceedings of the Twenty-First International Offshore and Polar Engineering Conference*. ISOPE2011, International Society of Offshore and Polar Engineers, pp. 275–282, URL <https://www.onepetro.org/conference-paper/ISOPE-I-11-508>.

Guérin, C.-A., Desmars, N., Grilli, S.T., Ducrozet, G., Perignon, Y., Ferrant, P., 2019. An improved Lagrangian model for the time evolution of nonlinear surface waves. *J. Fluid Mech.* 876, 527–552, URL <https://doi.org/10.1017/jfm.2019.519>.

Hansen, P.C., 2000. The l-curve and its use in the numerical treatment of inverse problems. In: *Computational Inverse Problems in Electrocardiology*. WIT Press, pp. 119–142, URL <https://www.sintef.no/globalassets/project/evitameeting/2005/lcurve.pdf>.

Hilmer, T., Thornhill, E., 2015. Observations of predictive skill for real-time Deterministic Sea Waves from the WaMoS II. In: *OCEANS 2015 - MTS/IEEE Washington*. pp. 1–7, URL <https://doi.org/10.23919/OCEANS.2015.7404496>.

Kabel, T., Georgakis, C.T., Rod Zeeberg, A., 2019. Mapping ocean waves using new LIDAR equipment. In: *Proceedings of the Twenty-Ninth (2019) International Ocean and Polar Engineering Conference*. International Society of Offshore and Polar Engineers, pp. 2558–2562, URL <https://www.onepetro.org/conference-paper/ISOPE-I-19-318>.

Klein, M., Dudek, M., Clauss, G., Ehlers, S., Behrendt, J., Hoffmann, N., Onorato, M., 2020. On the deterministic prediction of water waves. *Fluids* 5 (9), URL <https://doi.org/10.3390/fluids5010009>.

Köllisch, N., Behrendt, J., Klein, M., Hoffmann, N., 2018. Nonlinear real time prediction of ocean surface waves. *Ocean Eng.* 157, 387–400, URL <http://www.sciencedirect.com/science/article/pii/S0029801818303184>.

Kusters, J.G., Cockrell, K.L., Connell, B.S.H., Rudzinsky, J.P., Vinciullo, V.J., 2016. FutureWaves™: A real-time Ship Motion Forecasting system employing advanced wave-sensing radar. In: *OCEANS 2016 MTS/IEEE Monterey*. pp. 1–9, URL <https://doi.org/10.1109/OCEANS.2016.7761478>.

Li, G., Weiss, G., Mueller, M., Townley, S., Belmont, M.R., 2012. Wave energy converter control by wave prediction and dynamic programming. *Renew. Energy* 48, 392–403, URL <http://www.sciencedirect.com/science/article/pii/S0960148112003163>.

Ma, Y., Sclavounos, P.D., Cross-Whiter, J., Arora, D., 2018. Wave forecast and its application to the optimal control of offshore floating wind turbine for load mitigation. *Renew. Energy* 128, 163–176, URL <http://www.sciencedirect.com/science/article/pii/S0960148118305809>.

Naaijen, P., Trulsen, K., Blondel-Coupré, E., 2014. Limits to the extent of the spatio-temporal domain for deterministic wave prediction. *Int. Shipbuild. Prog.* 61 (3–4), 203–223, URL <https://doi.org/10.3233/ISIP-140113>.

Naaijen, P., Van Oosten, K., Roosen, K., Van't Veer, R., 2018. Validation of a deterministic wave and ship motion prediction system. In: *International Conference on Offshore Mechanics and Arctic Engineering*, Volume 7B: Ocean Engineering. pp. 1–8, V07BT06A032. URL <https://doi.org/10.1115/OMAE2018-78037>.

Nieto Borge, J.C., Rodríguez, G.R., Hessner, K., González, P.I., 2004. Inversion of marine radar images for surface wave analysis. *J. Atmos. Ocean. Technol.* 21 (8), 1291–1300, URL [https://doi.org/10.1175/1520-0426\(2004\)021<1291:OMRIF>2.0.CO;2](https://doi.org/10.1175/1520-0426(2004)021<1291:OMRIF>2.0.CO;2).

Noguier, F., Grilli, S.T., Guérin, C.-A., 2014. Nonlinear ocean wave reconstruction algorithms based on spatiotemporal data acquired by a flash LIDAR camera. *IEEE Trans. Geosci. Remote Sens.* 52 (3), 1761–1771, URL <https://doi.org/10.1109/TGRS.2013.2254494>.

- Nouguier, F., Guérin, C.-A., Chapron, B., 2009. “Choppy wave” model for nonlinear gravity waves. *J. Geophys. Res.* 114, 1–16, URL <https://doi.org/10.1029/2008JC004984>.
- Nouguier, F., Guérin, C.-A., Chapron, B., 2010. Scattering from nonlinear gravity waves: the “choppy wave” model. *IEEE Trans. Geosci. Remote Sens.* 48 (12), 4184–4192, URL <https://doi.org/10.1109/TGRS.2010.2050694>.
- Qi, Y., Wu, G., Liu, Y., Kim, M.-H., Yue, D.K.P., 2018a. Nonlinear phase-resolved reconstruction of irregular water waves. *J. Fluid Mech.* 838, 544–572, URL <https://doi.org/10.1017/jfm.2017.904>.
- Qi, Y., Wu, G., Liu, Y., Yue, D.K., 2018b. Predictable zone for phase-resolved reconstruction and forecast of irregular waves. *Wave Motion* 77, 195–213, URL <http://www.sciencedirect.com/science/article/pii/S0165212517301518>.
- Seiffert, B.R., Ducrozet, G., 2018. Simulation of breaking waves using the high-order spectral method with laboratory experiments: wave-breaking energy dissipation. *Ocean Dyn.* 68 (1), 65–89, URL <https://doi.org/10.1007/s10236-017-1119-3>.
- Seiffert, B.R., Ducrozet, G., Bonnefoy, F., 2017. Simulation of breaking waves using the high-order spectral method with laboratory experiments: Wave-breaking onset. *Ocean Model.* 119, 94–104, URL <http://www.sciencedirect.com/science/article/pii/S1463500317301427>.
- Simanesev, A., Trulsen, K., Krogstad, H.E., Nieto Borge, J.C., 2017. Surface wave predictions in weakly nonlinear directional seas. *Appl. Ocean Res.* 65, 79–89, URL <http://www.sciencedirect.com/science/article/pii/S0141118716303613>.
- Sviridov, S.A., 1993. States of arts on laser remote sensing techniques of sea surface roughness in Russia. In: *Proceedings of OCEANS '93*, Vol. 1. pp. 1473–1481, URL <https://doi.org/10.1109/OCEANS.1993.325957>.
- Trulsen, K., Stansberg, C.T., 2001. Spatial evolution of water surface waves: Numerical simulation and experiment of bichromatic waves. In: *Proceedings of the Eleventh International Offshore and Polar Engineering Conference*, Vol. 3. International Society of Offshore and Polar Engineers, pp. 71–77, URL <https://www.onepetro.org/conference-paper/ISOPE-I-01-247>.
- Wu, G., 2004. Direct Simulation and Deterministic Prediction of Large-scale Nonlinear Ocean Wave-field (Ph.D. thesis). Massachusetts Institute of Technology, URL <http://hdl.handle.net/1721.1/33450>.
- Zhang, J., Chen, L., Ye, M., Randall, R.E., 1996. Hybrid wave model for unidirectional irregular waves—part I. Theory and numerical scheme. *Appl. Ocean Res.* 18 (2), 77–92, URL <http://www.sciencedirect.com/science/article/pii/0141118796000090>.
- Zhang, J., Yang, J., Wen, J., Prislun, I., Hong, K., 1999. Deterministic wave model for short-crested ocean waves: Part I. Theory and numerical scheme. *Appl. Ocean Res.* 21 (4), 167–188, URL <http://www.sciencedirect.com/science/article/pii/S0141118799000115>.